

Ultrafast Optical Pulse Shaping using Dielectric Metasurfaces

Shawn Divitt^{1,2†}, Wenqi Zhu^{1,2†}, Cheng Zhang^{1,2†}, Henri J. Lezec^{1*} and Amit Agrawal^{1,2*}

¹Physical Measurement Laboratory, National Institute of Standards and Technology, Gaithersburg, MD 20899 USA

²Maryland Nanocenter, University of Maryland, College Park, MD 20742 USA

*Corresponding authors. e-mail: amit.agrawal@nist.gov, henri.lezec@nist.gov

[†]equal author contribution

One Sentence Summary: Simultaneous amplitude, phase and polarization modulation of ultrafast optical pulses is achieved using a dielectric metasurface.

Abstract: Remarkable advances in ultrafast lasers, chirped pulse amplifiers and frequency comb technology require fundamentally new pulse modulation strategies capable of supporting unprecedentedly large bandwidth and high peak power while maintaining high spectral resolution. Here, we demonstrate of optical pulse shaping using a dielectric metasurface able to simultaneously control the amplitude, phase and polarization of the various frequency components of an ultrafast pulse. Dielectric metasurfaces offer a low cost, high resolution, high diffraction efficiency, high damage threshold and integration-friendly alternative to commercial spatial-light-modulators used for controlling ultrafast pulses. By offering the potential for complete spatio-temporal control of optical fields, metasurface based pulse-shapers are expected to have significant impact in the field of ultrafast science and technology.

Development of ultrafast lasers that produce a train of optical pulses in the time-domain, or equivalently a comb of closely spaced spectral lines in the frequency-domain, have led to revolutionary advances in areas such as high-field physics (1), quantum optics (2, 3) and frequency metrology (4). These advances have been enabled by the development of techniques that began with dispersion compensation (5, 6) and eventually achieved customizable shaping of pulses with approaches in both the time (7, 8) and frequency domains (9–13). Because of the broadband nature of ultrafast pulses, the most common embodiment of pulse shaping involves some form of dispersion engineering – this includes both dispersion compensation to achieve transform-limited pulses for applications in long-distance communications (14) or nonlinear microscopy (15, 16), and pulse stretching that makes techniques such as chirped pulse amplification possible (17). Furthermore, arbitrary control over the phase and amplitude of individual comb lines enables optical arbitrary waveform generation (18, 19), which promises to have tremendous impact in applications such as coherent manipulation of quantum-mechanical processes (20–23), frequency-comb spectroscopy (24, 25), and ultrafast communications (26). Among the various pulse shaping techniques, Fourier-transform pulse shaping, which synthesizes optical pulses through parallel manipulation of spatially separated spectral components, has been the most widely adopted (10–12). This form of pulse shaping typically employs a liquid-crystal based spatial light modulator (SLM), which offers dynamic control over the optical amplitude and phase. However, SLMs are often bulky, costly, and limited in spectral resolution due to the finite pixel size and pixel density (27, 28).

Recently, dielectric metasurfaces – ultrathin, planar optical elements composed of an array of deep-subwavelength nanostructures – have emerged as a powerful technology for arbitrary

control over the amplitude, phase and polarization of light for spatial-domain wavefront manipulation in a compact platform (29–33). Here, we implement and demonstrate a metasurface that can control the temporal profile of light through coherent control of its constituent frequency components. This control is demonstrated by using a metasurface made of deep-subwavelength dielectric pillars, patterned and positioned with nanometer precision, to simultaneously control the spectral amplitude, phase and polarization of the various frequency components that constitute an ultrafast pulse, leading to temporal shaping of the pulse with arbitrary flexibility. Two classes of pulse-shaping metasurfaces with increasingly complex functionality are explored. The first class is a set of phase-manipulating metasurfaces that impart, through phase shift that are quadratic or higher order functions of frequency, the equivalent of anomalous dispersion enabling pulse compression or stretching. The second class simultaneously manipulates both phase and amplitude to achieve precise control over the temporal profile of a pulse, for example to split one pulse into two.

A Fourier transform setup (Fig. 1A), in which an optical pulse is first angularly dispersed by a grating and then focused by an off-axis metallic parabolic mirror (see Methods and Supplementary Figure S1), is used to spatially map the spectral components of the optical pulse onto the full length of one or more cascaded metasurface matrices ($S_{i=1}$ to $S_{i=n}$, schematically illustrated in Fig. 1A) each consisting of m different metasurfaces ($M_{i,j=1}$ to $M_{i,j=m}$). A given metasurface ($M_{i,j}$) is designed to treat in parallel the broad range of frequencies (ω_k for $k = 1$ to N) constituting the pulse by implementing a spatially dependent, one-dimensional custom masking function $m_i(x)$ (discretized to N individual sectors, one for each ω_k , Fig. 1B). This function operates on either phase alone or both phase and amplitude, where each wavelength λ is mapped to a specific lateral position x (Fig. 1A). This mapping follows a quasi-linear function $\lambda(x)$ (see

Supplementary Figure S2). A polarizing metasurface element can also be inserted in the beam path to help achieve the required net masking function. After passing through the metasurfaces and undergoing local phase, amplitude and polarization transformations, the spectral components of the beam are recombined using a second parabolic mirror and grating pair, yielding a shape-modified pulse with the desired temporal characteristics. The metasurfaces are illuminated using a Ti:Sapphire oscillator generating $\lesssim 10$ fs pulses, centered at 800 nm (FWHM bandwidth of ≈ 60 THz), with a repetition rate of 75 MHz and pulse energy of 6.5 nJ. The characteristics of the recombined pulse exiting the system, *i.e.* spectral amplitude and phase, are measured using the technique of spectral phase interferometry for direct electric-field reconstruction (SPIDER) (34).

The metasurface consists of nanopillars of polycrystalline silicon arrayed on a fused-silica substrate. The nanopillars are fabricated by patterning the silicon, which was deposited on the substrate by low-pressure chemical vapor deposition (LPCVD), using electron-beam lithography followed by reactive ion etching (see Methods). The nanopillars have a height $H = 660$ nm and a rectangular cross-section, where length L_x and width L_y range from 70 nm to 250 nm, and have a subwavelength spacing p ranging from 280 nm to 615 nm. Polycrystalline silicon was selected for its high damage threshold (35), large refractive index and low optical absorption in the near-infrared spectral range (Supplementary Figure S3) whereas fused-silica was selected for its low refractive index, low optical dispersion, and isotropy. The total length of any metasurface in this work along the x -axis, 3 cm, was chosen to match the spectral dispersion length in the Fourier plane to the full bandwidth of the pulse as set by grating pitch, off-axis parabolic mirror curvature and grating-mirror distance (accommodating the quasi-linear mapping $\lambda(x)$ of slope 8.78 nm/mm). The number of individual metasurface elements in one row along the x -direction is approximately 10^5 , resulting in about 8 comb-lines per element for a pulse dispersed over its full bandwidth and

corresponding to a theoretically achievable lower limit on the spectral resolution of ≈ 600 MHz. However, optical aberrations and the diffraction caused by the finite size of the optics in our case limits the spectral resolution to ≈ 150 GHz (corresponding to the number of independently controllable spectral features $N \approx 600$). The metasurface width along the y -axis of $300 \mu\text{m}$ is chosen to contain the vertical spread of the loosely-focused ($\text{NA} \approx 0.026$) spectrally dispersed beam at the Fourier plane (see Methods). The spectrally-averaged transmission power varies between 50-98 % per metasurface, with an average of approximately 80%. A typical 4 %-per-substrate-surface loss is also present due to reflections.

A metasurface can be designed to control the dispersion of an ultrafast pulse through manipulation of its spectral phase alone. Here we implement a metasurface matrix, $S_{i=1}$, bearing a discrete number j of different metasurfaces stacked in the y -direction, each with a masking function $m_{1,j}(x)$ and accessed by a mechanical translation $\Delta Y_{1,j}$ of the upper edge of the sample relative to the plane of the beam (Fig. 2A). By giving each metasurface pillar a square cross-section ($L_x = L_y = L$), and setting $L(x)$ to a specific value in the interval $[75 \text{ nm}, 210 \text{ nm}]$, a phase of any modulus between 0 and 2π can be imparted within the spectral bandwidth of the pulse with high transmittance (Fig. 2B and Supplementary Figure S4), as calculated by rigorous coupled wave analysis (RCWA) (36). We first demonstrate how such a phase-control metasurface can convert a positively chirped optical pulse into a transform limited pulse, by conferring a quadratic spectral phase-shift $\varphi_{1,j} = -A_{1,j}(\nu - \nu_0)^2$ to the pulse, where $\nu_0 = 375 \text{ THz}$ is the center frequency of the pulse and $A_{1,j}$ is a weighting factor (defined to be positive) that is intended to enable compensation of various degrees of dispersion. The spectral phase shift as a function of wavelength enabling compensation of lowest order dispersion for propagation through 5 mm of glass, $\varphi_{1,1}(\nu) = -A_{1,1}(\nu - \nu_0)^2$ where $A_{1,1} = 6 \times 10^{-3} \text{ rad/THz}^2$ is depicted by the white line of Fig. 2B; the

locus of this line yields a specific design value of L for each wavelength (also see Supplementary Figure S5). The metasurface pillar dimensions at each location x are then set using the look-up function, $L(v(x))$. Upon inserting the metasurface matrix S_1 into the Fourier transform setup, and translating the matrix to access metasurface $M_{1,1}$, the relative spectral phase shift conferred by the fabricated metasurface displays anomalous dispersion and closely replicates the designed phase profile (Fig. 2C). Providing this Fourier transform setup with an input of a positively chirped Gaussian optical pulse (of pulse length ≈ 100 fs, chirped by a ≈ 5 mm-thick glass slab) yields an output of a compressed, transform limited pulse (of length ≈ 10 fs, Fig. 2D). This demonstrates the ability of a single phase-only metasurface to compensate for normal dispersion via a tailored anomalous dispersion transformation. Additional higher order spectral shifts, for example cubic shifts, can be achieved by inserting, within the focal volume about the Fourier plane, an additional metasurface matrix $S_{i=2}$ composed of metasurfaces $M_{2,j'}$ characterized by $\varphi_{2,j'} = -A_{2,j'}(v - v_0)^3$. By translating metasurface $M_{2,2}$ to coincide with the plane of the beam via a shift $\Delta Y_{2,2}$ of S_2 (Fig. 2E) yields $A_{2,2} = 9 \times 10^{-5}$ rad/THz³ resulting in a net designed spectral phase shift for the system of φ_{net} , displayed in Fig. 2F along with individual quadratic and cubic components, respectively. The close approximate between φ_{net} and $(\varphi_{1,1} + \varphi_{2,2})$ indicates the linearity of the system. Propagating the transform-limited pulse through this additional cubic-phase masking function ($m_{2,2}$) results in a temporal pulse profile that is consistent with that expected for a pulse possessing a negatively chirped, linear group delay dispersion (Fig. 2G). The range of second- and third-order dispersion compensation made available by combining S_1 and S_2 is displayed in Supplementary Fig. S6. Nonlinear spectral phase distortions characteristic of high-energy pulse propagation through a dispersive medium could similarly be corrected using this cascaded metasurface approach in a dynamic manner.

A more general embodiment of a pulse shaper requires the ability to control simultaneously, and independently, both phase and amplitude of the spectral components of an ultrafast pulse (27, 37). We achieve this by implementing metasurfaces based on nanopillars of rectangular cross-section that can control the local phase (through the respective length L_x and width L_y of a given rectangle, as calculated by RCWA) and local polarization (through the rotation θ of the rectangle with respect to the x -axis – each pillar acting as a nanoscale half-wave plate) of a linearly polarized pulse (electric-field parallel to the x -axis). The combination of half-wave plates with a wire-grid linear polarizer (Supplementary Figure S7), here custom-fabricated on the exit side of the metasurface-bearing substrate (Fig. 3A), yields amplitude modulation set by θ (Fig. 3B). In general, the polarization state of any frequency component exiting the polarizer after passage through a given metasurface pillar rotated to angle θ can be expressed by the Jones vector (see Supplementary Text):

$$J = \begin{bmatrix} e^{i\varphi_x} \cos^2 \theta + e^{i\varphi_y} \sin^2 \theta \\ 0 \end{bmatrix}, \quad (1)$$

where φ_x and φ_y are the respective phase-shifts for $\theta = 0^\circ$ and 90° , respectively. Enforcing the half-waveplate condition, $\varphi_x - \varphi_y = \pm\pi$, then leads to a Jones vector for the final polarization state given by:

$$J = \begin{bmatrix} e^{i\varphi_x} \cos(2\theta) \\ 0 \end{bmatrix}, \quad (2)$$

yielding an x -polarized wave of amplitude and phase determined by independent variables, θ and φ_x , respectively. The exit phase through the half-waveplate stays constant as the pillar is rotated, as further confirmed by RCWA simulations of a three-dimensional unit cell incorporating the pillar (Fig. 3B and Methods).

Optimal half-waveplate performance is defined by maximum transmission amplitude and a relative phase $|\varphi_x - \varphi_y|$ as close as possible to π . This occurs for pillar lateral dimension pairs (L_x, L_y) which minimize the following figure-of-merit (*FOM*) function:

$$FOM = \left| \frac{t_x e^{i\varphi_x}}{t_y e^{i\varphi_y}} - e^{i\pi} \right|^2, \quad (3)$$

where t_x and t_y represent the transmission amplitude of a given pillar at $\theta = 0^\circ$ and 90° respectively. The parametric curves $f(L_x, L_y)$ representing the local minimum in the *FOM* can be numerically derived at each wavelength λ ; the representative curves at $\lambda = 800$ nm are indicated by the solid white lines of Fig. 3C. The range of permissible (L_x, L_y) combinations given by f at a given wavelength yields a set of available phase shifts φ_x spanning the full range $[0, 2\pi]$. This information is compiled into two look-up plots: $L_x(\varphi_x, \lambda)$ and $L_y(\varphi_x, \lambda)$ (Fig. 3D and Supplementary Figure S8) that, in combination with appropriate amplitude modulation set by pillar angle θ , can be used to design each metasurface element to achieve the desired masking function for pulse shaping via simultaneous control of spectral phase and amplitude. For example, a complex masking function characterized by a periodic spectral modulation via Fourier transformation translates into a time-shift convolution operation. An example pulse shaping operation enabled by such a complex masking function is to split a single optical pulse into two replicas time-separated by an interval ΔT . This operation requires simultaneous modulation of amplitude and phase over the entire spectral range of the pulse, with amplitude $t(\nu) = |g(\nu)|$, where $g(\nu) = \cos\{\pi(\nu - \nu_0)/\Delta\nu\}$ and $\Delta\nu = 1/\Delta T$ is the spectral period for t . The corresponding phase φ_x oscillates between 0 and π with dependence $\varphi_x(\lambda) = \pi(\text{sgn}(g(\nu)) + 1)/2$. The performance of a metasurface designed according to this strategy (Supplementary Figure S9) to achieve pulse doubling with target $\Delta T = 30$ fs, is illustrated in Fig. 3E-G, for a Gaussian input

pulse of length 10 fs. The asymmetry in the pulse is due to the deviation between the applied and designed phases. In its most general embodiment, a pulse shaper is required to control simultaneously, and independently, the phase, amplitude and polarization of the spectral components of an ultrafast pulse, ideally using a single optical element. In our case, this can simply be achieved by utilizing the additional degree-of-freedom provided by the multiple metasurface matrix elements arrayed in the y -direction.

In summary, we have demonstrated the ability to arbitrarily control the temporal profile of large bandwidth optical pulses using an integration-friendly, lithographically-patterned, ultrathin-dielectric metasurface platform, offering promise for numerous applications in the areas of high-energy physics, frequency-combs, quantum-optics and lightwave-communications. We expect that metasurface techniques can be extended into the full spatiotemporal domain wherein masking functions will concurrently modulate both the temporal and spatial characteristics of a pulse. Such an extension would allow for the creation of custom space-time fields that enable precise control over ultrafast pulse propagation through complex scattering media. By extending the metasurface configuration to accommodate two-dimensional spectral dispersion, we expect that the number of individually controllable spectral features can be increased by several orders of magnitude, thereby allowing line-by-line shaping with record bandwidth and resolution (13). Additionally, we expect that the inherent nonlinearity of the metasurface constituent dielectric materials will allow for direct line-by-line frequency conversion in the Fourier domain (38, 39). Expanding metasurfaces into the realm of time-domain manipulation will amplify the already significant impact of their application as two-dimensional wavefront shapers, and open new vistas in the field of ultrafast science and technology.

References and Notes:

1. T. Brabec, Ed., *Strong field laser physics* (Springer Series in Optical Sciences, 2009th Edi., 2009).
2. W. S. Warren, H. Rabitz, M. Dahleh, Coherent control of quantum dynamics - the dream is alive. *Science*. **259**, 1581–1589 (1993).
3. C. Brif, R. Chakrabarti, H. Rabitz, Control of quantum phenomena: past, present and future. *New J. Phys.* **12**, 075008 (2010).
4. J. Ye, S. T. Cundiff, *Femtosecond optical frequency comb technology* (Springer, 2005).
5. E. Treacy, Optical pulse compression with diffraction gratings. *IEEE J. Quantum Electron.* **5**, 454–458 (1969).
6. R. L. Fork, O. E. Martinez, J. P. Gordon, Negative dispersion using pairs of prisms. *Opt. Lett.* **9**, 150 (1984).
7. R. Szipöcs, C. Spielmann, F. Krausz, K. Ferencz, Chirped multilayer coatings for broadband dispersion control in femtosecond lasers. *Opt. Lett.* **19**, 201–203 (1994).
8. P. Tournois, Acousto-optic programmable dispersive filter for adaptive compensation of group delay time dispersion in laser systems. *Opt. Commun.* **140**, 245–249 (1997).
9. A. M. Weiner, J. P. Heritage, E. M. Kirschner, High-resolution femtosecond pulse shaping. *J. Opt. Soc. Am. B.* **5**, 1563 (1988).
10. M. A. Dugan, J. X. Tull, W. S. Warren, High-resolution acousto-optic shaping of unamplified and amplified femtosecond laser pulses. *J. Opt. Soc. Am. B.* **14**, 2348 (1997).
11. E. Zeek *et al.*, Pulse compression by use of deformable mirrors. *Opt. Lett.* **24**, 493–495 (1999).
12. A. M. Weiner, Femtosecond pulse shaping using spatial light modulators. *Rev. Sci. Instrum.* **71**, 1929–1960 (2000).
13. V. R. Supradeepa, C. Huang, D. E. Leaird, A. M. Weiner, Femtosecond pulse shaping in two dimensions: towards higher complexity optical waveforms. *Opt. Express*. **16**, 11878–11887 (2008).

14. P. Marin-Palomo *et al.*, Microresonator-based solitons for massively parallel coherent optical communications. *Nature*. **546**, 274–279 (2017).
15. N. Dudovich, D. Oron, Y. Silberberg, Single-pulse coherently controlled nonlinear Raman spectroscopy and microscopy. *Nature*. **418**, 512–514 (2002).
16. M. Pawłowska *et al.*, Shaping and spatiotemporal characterization of sub-10-fs pulses focused by a high-NA objective. **22**, 17256–17264 (2014).
17. D. Strickland, G. Mourou, Compression of amplified chirped optical pulses. *Opt. Commun.* **56**, 219–221 (1985).
18. Z. H. I. Jiang, C. Huang, D. E. Leaird, A. M. Weiner, Optical arbitrary waveform processing of more than 100 spectral comb lines. *Nat. Photonics*. **1**, 463–467 (2007).
19. S. T. Cundiff, A. M. Weiner, Optical arbitrary waveform generation. *Nat. Photonics*. **4**, 760–766 (2010).
20. A. M. Weiner, D. E. Leaird, G. P. Wiederrecht, K. A. Nelson, Femtosecond pulse sequences used for optical manipulation of molecular motion. *Science*. **247**, 1317–1319 (1990).
21. A. Assion *et al.*, Control of chemical reactions by feedback-optimized phase-shaped femtosecond laser pulses. *Science*. **282**, 919–922 (1998).
22. T. Brixner, N. H. Damrauer, P. Niklaus, G. Gerber, Photosensitive adaptive femtosecond quantum control in the liquid phase. *Nature*. **414**, 57–60 (2001).
23. R. J. Levis, G. M. Menkir, H. Rabitz, Selective bond dissociation and rearrangement with optimally tailored, strong-field laser pulses. *Science*. **292**, 709–713 (2001).
24. A. Marian, M. C. Stowe, J. R. Lawall, D. Felinto, J. Ye, United time-frequency spectroscopy for dynamics and global structure. *Science*. **306**, 2063–2068 (2004).
25. S. A. Diddams, L. Hollberg, V. Mbele, Molecular fingerprinting with the resolved modes of a femtosecond laser frequency comb. *Nature*. **445**, 627–630 (2007).
26. I. S. Lin, J. D. McKinney, A. M. Weiner, Photonic synthesis of broadband microwave arbitrary waveforms applicable to ultra-wideband communication. *IEEE Microw. Wirel. Components Lett.* **15**, 226–228 (2005).

27. M. Plewicki, F. Weise, S. M. Weber, A. Lindinger, Phase, amplitude, and polarization shaping with a pulse shaper in a Mach–Zehnder interferometer. *Appl. Opt.* **45**, 8354–8359 (2006).
28. J. J. Field, T. A. Planchon, W. Amir, C. G. Durfee, J. A. Squier, Characterization of a high efficiency, ultrashort pulse shaper incorporating a reflective 4096-element spatial light modulator. *Opt. Commun.* **278**, 368–376 (2007).
29. D. Lin, P. Fan, E. Hasman, M. L. Brongersma, Dielectric gradient metasurface optical elements. *Science*. **345**, 298–302 (2014).
30. A. Arbabi, Y. Horie, M. Bagheri, A. Faraon, Dielectric metasurfaces for complete control of phase and polarization with subwavelength spatial resolution and high transmission. *Nat. Nanotechnol.* **10**, 937–943 (2015).
31. M. Khorasaninejad *et al.*, Metalenses at visible wavelengths: Diffraction-limited focusing and subwavelength resolution imaging. *Science*. **352**, 1190–1194 (2016).
32. M. Khorasaninejad, F. Capasso, Metalenses: Versatile multifunctional photonic components. *Science*. **358**, 1146 (2017).
33. S. M. Choudhury *et al.*, Material platforms for optical metasurfaces. *Nanophotonics*. **7**, 959–987 (2018).
34. C. Iaconis, I. A. Walmsley, Spectral phase interferometry for direct electric-field reconstruction of ultrashort optical pulses. *Opt. Lett.* **23**, 792–794 (1998).
35. Y. Zhao *et al.*, Engineering the thermal conductivity along an individual silicon nanowire by selective helium ion irradiation. *Nat. Commun.* **8**, 15919 (2017).
36. V. Liu, S. Fan, S4: A free electromagnetic solver for layered periodic structures. *Comput. Phys. Commun.* **183**, 2233–2244 (2012).
37. F. Weise, A. Lindinger, Full control over the electric field using four liquid crystal arrays. *Opt. Lett.* **34**, 1258–1260 (2009).
38. Y. Yang *et al.*, Nonlinear Fano-resonant dielectric metasurfaces. *Nano Lett.* **15**, 7388–7393 (2015).
39. L. Wang *et al.*, Nonlinear wavefront control with all-Dielectric metasurfaces. *Nano Lett.*

Lett. **18**, 3978–3984 (2018).

Acknowledgments: S. D., W. Z., C. Z. and A. A. acknowledge support under the Cooperative Research Agreement between the University of Maryland and the National Institute of Standards and Technology Center for Nanoscale Science and Technology, Award#70NANB14H209, through the University of Maryland. We thank Prof. Ting Xu and Dr. Yuzhang Liang from Nanjing University, Dr. Amit Solanki and Prof. Fawwaz Habbal from Harvard University for helpful discussions.

Supplementary Materials:

Materials and Methods

Supplementary Text

Figs. S1 to S9

Figure Captions

Fig. 1. Optical pulse shaping using cascaded metasurfaces. (A) Schematic diagram of a Fourier transform pulse shaping setup, consisting of a pair of diffraction gratings (G_1 and G_2), a pair of parabolic mirrors (PM_1 and PM_2), and a cascaded sequence of metasurfaces matrices S_i ($i = 1, 2, \dots, n$). Each matrix S_i consists of m different metasurfaces ($M_{i,j=1}$ to $M_{i,j=m}$). An input optical pulse upon propagation through this setup is transformed into a shape-modified output pulse of tailored temporal characteristics. (B) Pulse shaping at the Fourier plane of the setup. A given metasurface $M_{i,j}$ is discretized to N individual sectors to treat in parallel the broad range of frequencies (ω_k for $k = 1$ to N), imparting a complex transfer function $t_{i,k}e^{i\varphi_{i,k}}$ for each ω_k . The spectral components of the input pulse are treated in parallel through a location specific effective masking function of complex amplitude $t_k e^{i\varphi_k}$, where $t_k = \prod_{i=1}^n t_{i,k}$ and $\varphi_k = \sum_{i=1}^n \varphi_{i,k}$.

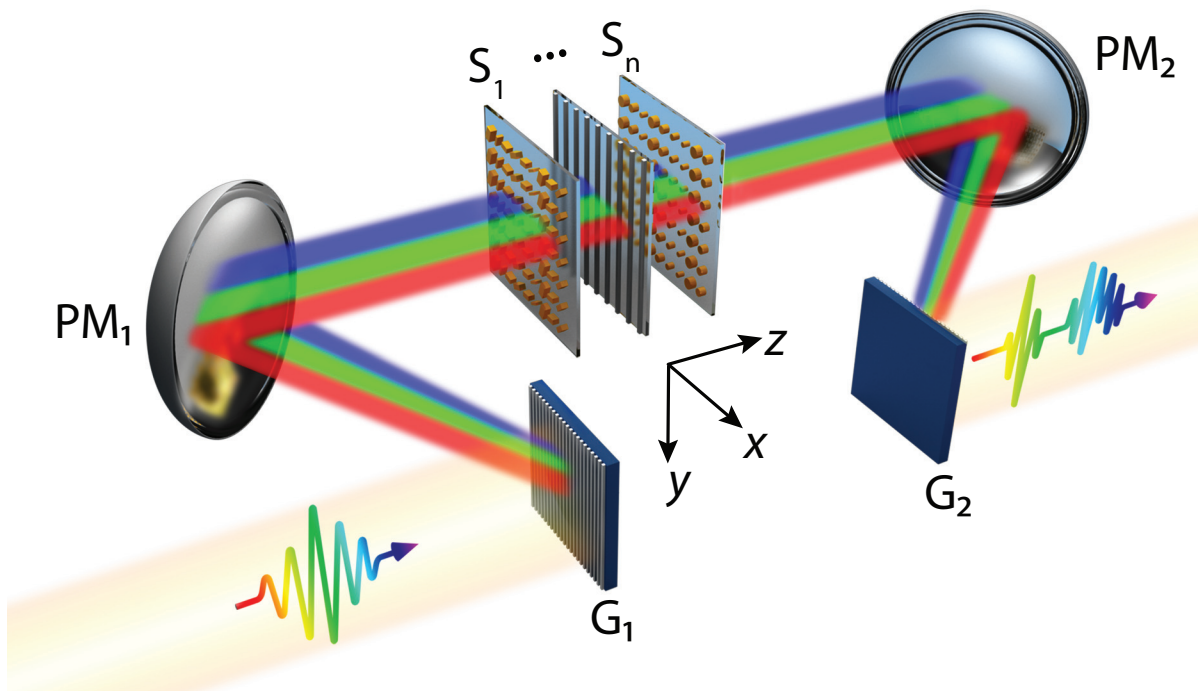
Fig. 2. Femtosecond pulse shaping using phase modulating metasurfaces. (A) Schematic diagram of a spectrally dispersed pulse propagating through a specific metasurface $M_{1,1}$ of a metasurface matrix S_1 , including a magnified schematic of a unit-cell consisting of a Si nanopillar on glass. The nanopillars have a square cross-section with a position dependent side-length $L(x)$ and constant height H . Inset: A representative scanning electron microscope (SEM) image of the metasurface. Scale bar represents 500 nm. (B) A color-map depicting the values of L required to achieve an arbitrary phase $\varphi(\text{mod}, 2\pi)$ at any wavelength λ , calculated using the RCWA method. The overlaid white line represents a spectral phase function $M_{1,1}$ targeted to compensate the lowest order dispersion upon pulse-propagation through 5 mm of glass, yielding a quadratic function in frequency with anomalous spectral dependence $\varphi_{1,1}(\nu) = -A_{1,1}(\nu - \nu_0)^2$, where $A_{1,1} = 6 \times 10^{-3} \text{ rad/THz}^2$, and $\nu_0 = 375 \text{ THz}$ is the center frequency. (C, D) Experimental pulse shaping using fabricated metasurface $M_{1,1}$ that implements masking function $m_{1,1}(x) = e^{i\varphi_{1,1}(\nu(x))}$, where C represents the measured spectral phase conferred by the metasurface (solid green) and a 5 mm-thick glass (solid blue), and D represents metasurface-induced pulse compression (solid red) of a positively chirped Gaussian optical pulse (solid blue) to its transform limit (T.L., dashed yellow). (E) Schematic diagram of a spectrally dispersed pulse propagating through two cascaded metasurfaces $M_{1,1}$ and $M_{2,2}$ located on separate metasurface matrices S_1 and S_2 respectively, where the top edge of each matrix is shifted from the plane of the beam by

distances $\Delta Y_{1,1}$ and $\Delta Y_{2,2}$ respectively. **(F)** Experimental pulse shaping using cascaded metasurfaces $M_{1,1}$ and $M_{2,2}$ where $M_{1,1}$ is the quadratic metasurface of **C**, and $M_{2,2}$ implements a cubic masking function $m_{2,2}(x) = e^{i\varphi_{2,2}(v(x))}$, where $\varphi_{2,2}(v) = -A_{2,2}(v - v_0)^3$ and $A_{2,2} = 9 \times 10^{-5} \text{ rad/THz}^3$. The measured spectral phases conferred by the metasurfaces individually ($M_{1,1}$ as solid green, $M_{2,2}$ as solid cyan, and the numerical summation of the two as dashed black) and in cascade (solid magenta) are shown. **(G)** The measured (solid purple) and designed (dashed purple) temporal profile of the output pulse resulting from transformation of the chirped input pulse of **C** (solid red) by the cascaded quadratic and cubic metasurfaces. The temporal pulse profile is consistent with that expected for a pulse possessing a cubic spectral phase function (dashed purple). The random error in measuring the spectral phase using SPIDER is within the linewidth of the plots.

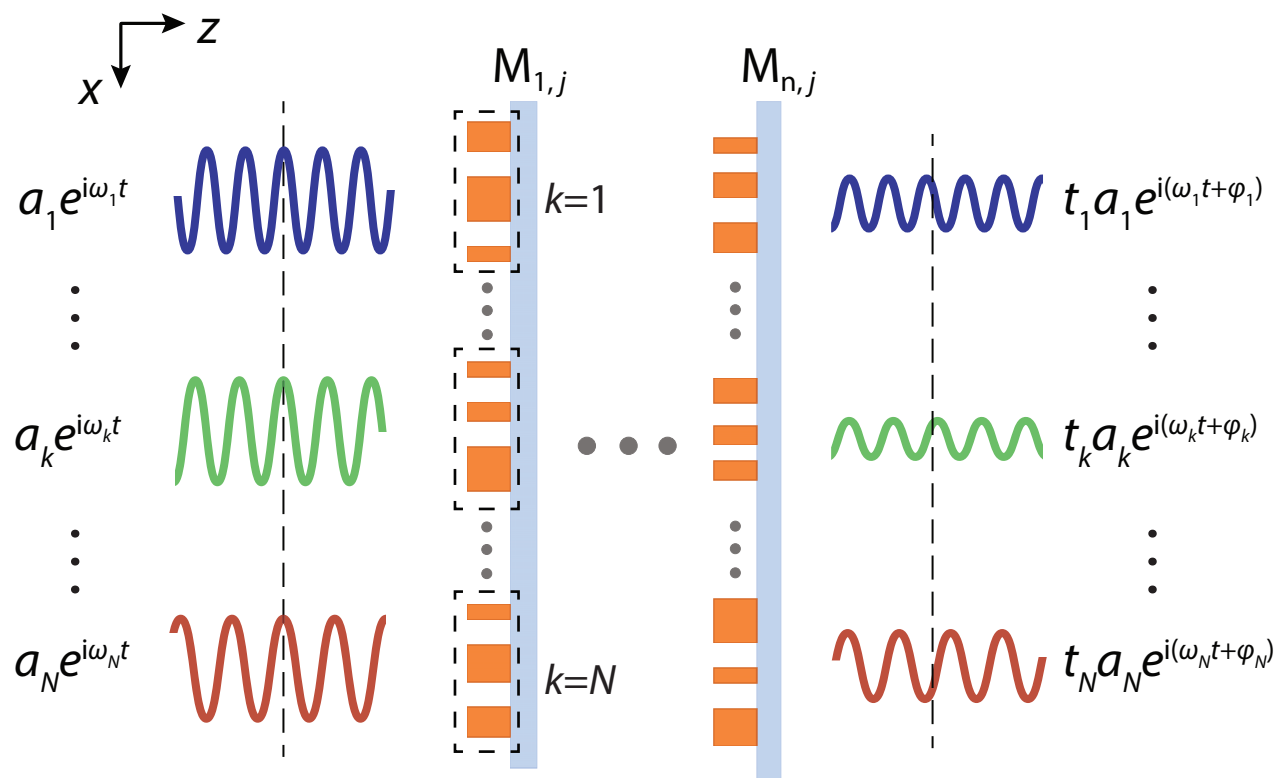
Fig. 3. Femtosecond pulse shaping using simultaneous phase and amplitude modulating metasurfaces. **(A)** Schematic diagram of an integrated device consisting of (i) a metasurface composed of rectangular Si nanopillars (of position dependent length L_x , width L_y , and rotation angle θ , and uniform height $H = 660 \text{ nm}$) on glass acting as nanoscale half-wave plates, and (ii) a wire-grid linear polarizer (pitch p_2) on the opposite side of the glass substrate – able to control simultaneously the phase and amplitude of the spectral components of a linearly polarized input pulse. Inset: A representative SEM image of the metasurface. Scale bar represents 500 nm. **(B)** RCWA calculated amplitude and phase of the conferred transmission factor for a pillar ($L_x = 182 \text{ nm}$ and $L_y = 98 \text{ nm}$) at $\lambda = 800 \text{ nm}$ as a function of θ . **(C)** Color plot: an example of the figure-of-merit (FOM) quantifying the half-wave plate performance of the nanopillars as a function of L_x and L_y , displayed here for $\lambda = 800 \text{ nm}$. The overlaid solid white lines depict the parametric curves $f(L_x, L_y)$ representing the local minima in FOM . **(D)** Color-maps depicting the values of L_x and L_y respectively, required to achieve an arbitrary phase $\varphi_x(\text{mod}, 2\pi)$ at any wavelength λ . The overlaid solid white lines represents the spectral phase function required to split an optical pulse into two time-separated replicas with separation $\Delta T = 30 \text{ fs}$. **(E, F, G)** Experimental demonstration of pulse splitting, for an input Gaussian pulse of length 15 fs. **E** and **F** display respectively the measured spectral phase φ_x and transmission amplitude t conferred by the metasurface/polarizer combination along with the targeted design curves. **G** represents the measured temporal profile of the split pulse (solid red), along with the targeted profile (solid blue) for a Gaussian input pulse

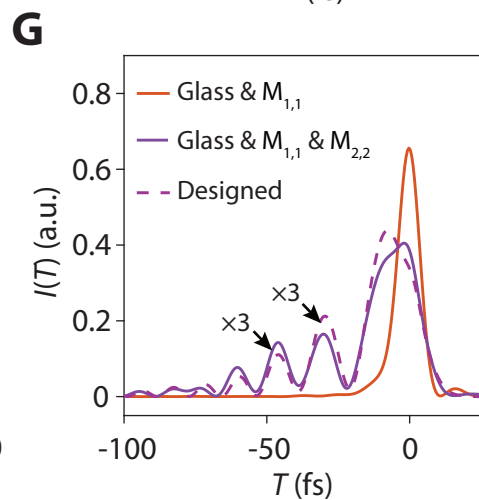
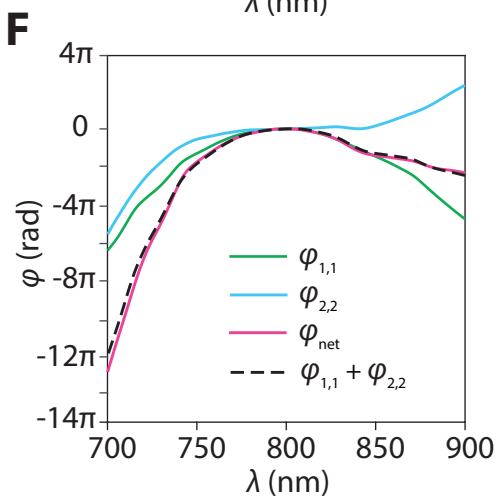
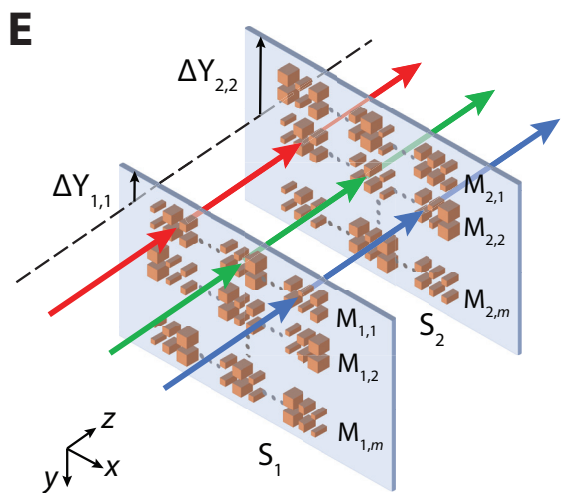
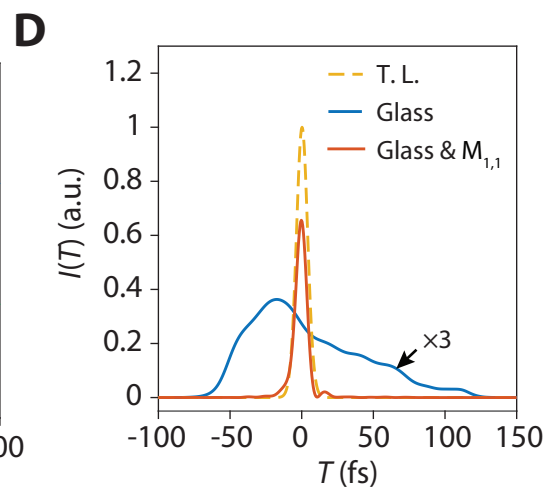
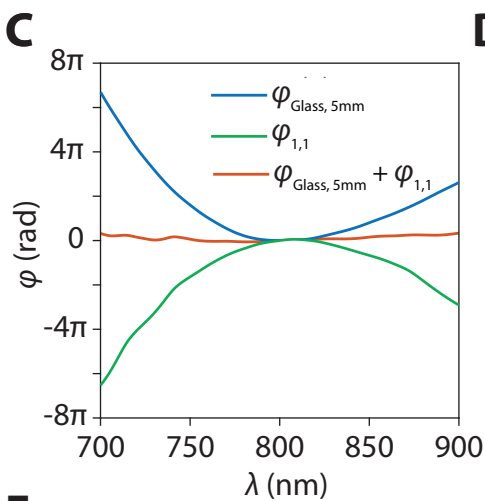
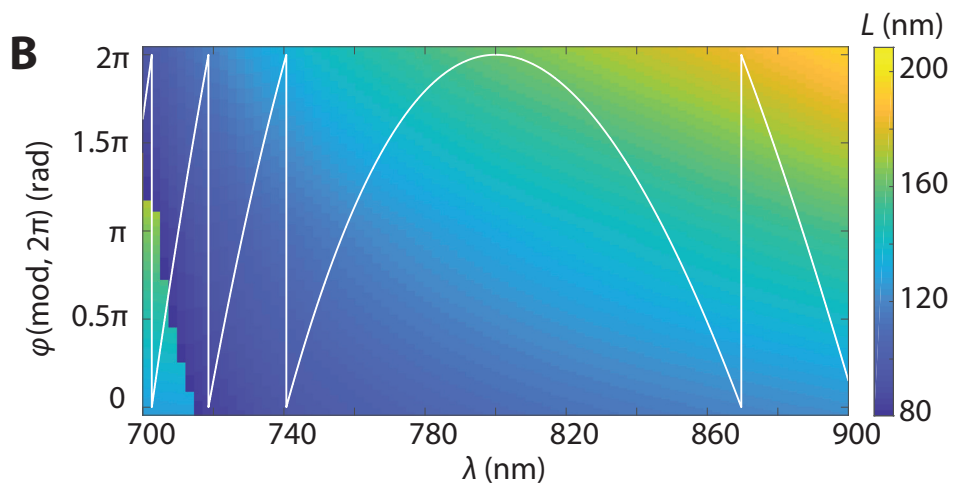
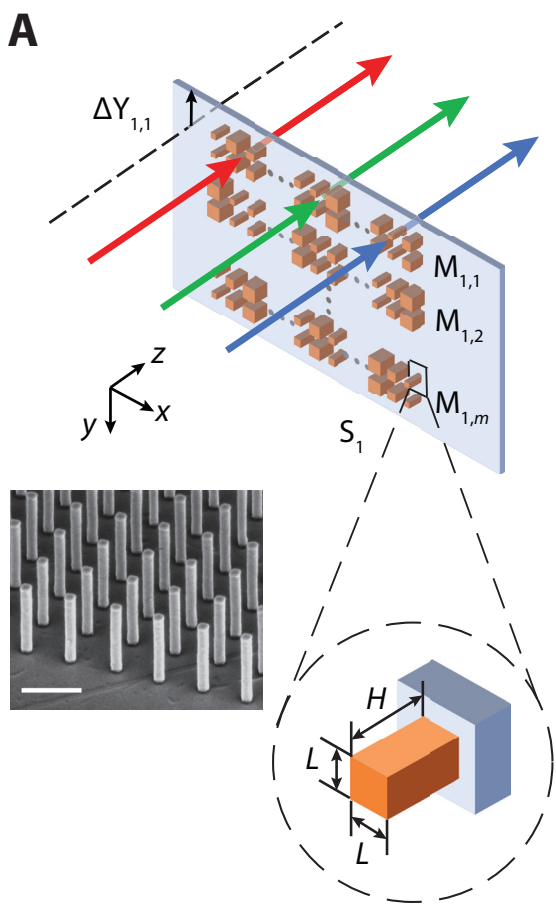
(dashed yellow). The random error in measuring the spectral phase and amplitude using SPIDER is within the linewidth of the plots.

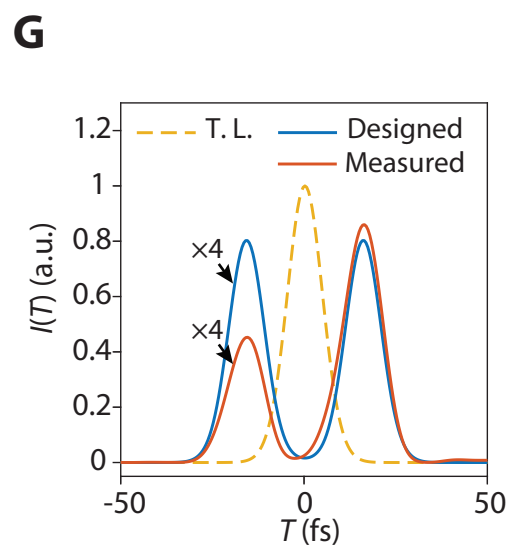
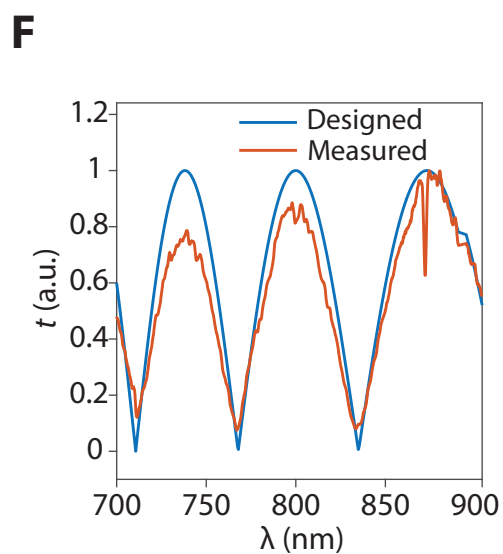
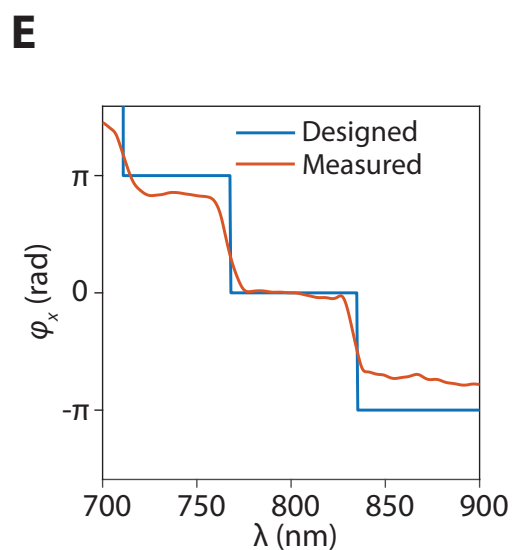
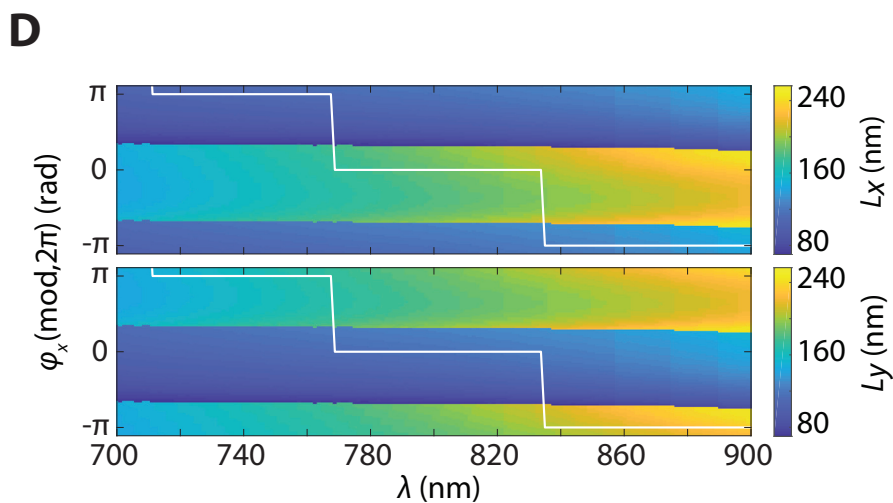
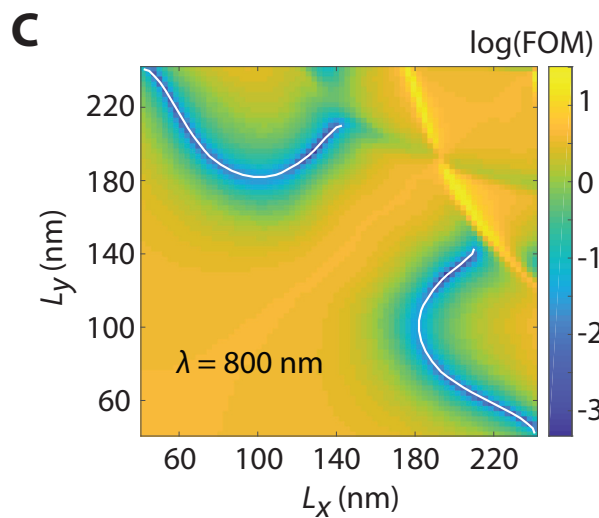
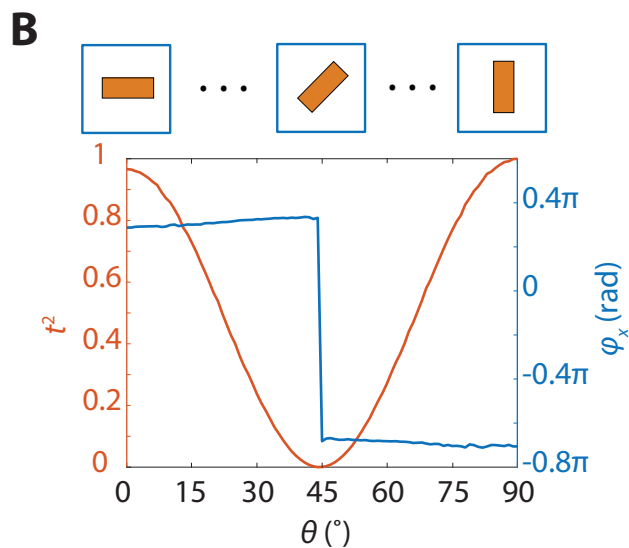
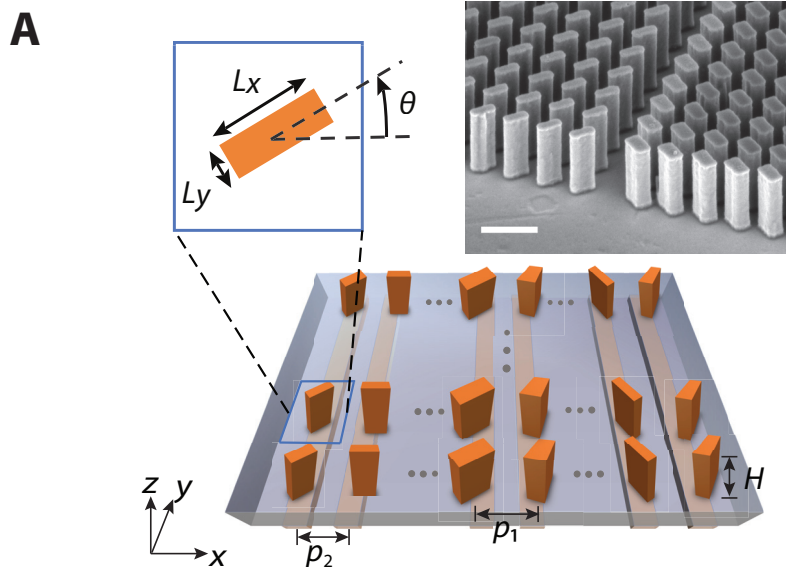
A



B







Materials and Methods

Metasurface fabrication

As a first step in the fabrication of the Si metasurface, a layer of 660-nm-thick polycrystalline silicon was deposited onto a fused silica wafer via low pressure chemical vapor deposition (LPCVD). Two 100-nm-thick layers of poly-methyl methacrylate (PMMA), namely PMMA 495 and PMMA 950, were consecutively spin coated on Si for electron beam lithography (EBL). A layer of 20-nm-thick Al was also deposited on top of PMMA bilayer via thermal evaporation prior to the EBL to avoid charging effects. PMMA bilayer was then exposed under a 100 keV electron beam, developed for 90 s in methyl isobutyl ketone (MIBK), and rinsed for 30 s in isopropyl alcohol (IPA). After EBL, a layer of 40 nm-thick Al was deposited onto the sample via electron-beam evaporation for lift-off. Using this layer of Al as an etch mask, inductively-coupled-plasma reactive ion etching (ICP-RIE) were performed to etch the Si layer at 15 °C, forming standing Si nanowires with high aspect ratio. This ICP-RIE recipe uses a gas mixture of SF₆ and C₄F₈, with ICP power of 1200 W and radio frequency (RF) power of 15 W. The fabrication is finalized by sequentially soaking the wafer in post-etch residue remover (80 °C for 30 minutes) and Type-A aluminum etchant (40 °C for 4 minutes) to remove the etch residue and the Al etch mask, respectively.

Polarizer fabrication

A 150-nm-thick Al layer was deposited on the fused silica substrate using electron beam evaporation. Afterwards, a layer of 300-nm-thick PMMA was coated on the Al layer and patterned into 500-μm-long lines with a period of 200 nm and linewidth of 70 nm, arrayed over an area of 500 μm by 4 cm to be readily aligned with the entire metasurface area. The line patterns in the PMMA layer were transferred into the Al layer via ICP-RIE, which was performed with a gas mixture of BCl₃, CH₄, and Cl₂, ICP power of 300 W, and RF power of 100 W. Finally, the PMMA etch mask was removed by solvent.

Phase modulating metasurface design:

The color-map depicting the values of L required to achieve an arbitrary phase $\phi(\text{mod}, 2\pi)$ at any wavelength λ is calculated at $N = 401$ discrete wavelengths given by $\lambda_k = (k + 800)$ nm, where k is an integer varying from -200 to 200 (shown in Fig. 1B). The phase modulating metasurfaces consisted of Si pillars of square cross-section of side-length L ranging from $0.15p_i$ to $0.85p_i$, where p_i is the pitch of the unit cell. For each discrete wavelength λ_i , p_i is chosen to be $p_i = \lambda_i/1.45$. Using the color map of Fig. 2B, along with the wavelength λ to lateral-location x mapping (given approximately by the linear function $\lambda(x)$ of slope -8.78 nm/mm, the metasurface layout consisting of square pillars of lateral location dependent lengths $L(x)$ can be designed to impose any arbitrary spectral phase $\phi_{i,j}$.

Simultaneous phase and amplitude modulating metasurfaces design:

Color-maps depicting the values of L_x and L_y respectively, required to achieve an arbitrary phase $\phi_x(\text{mod}, 2\pi)$ is calculated at 401 discrete wavelengths given by $\lambda_k = (k + 800)$ nm, where k is an integer varying from -200 to 200 (shown in Fig. 3D). The simultaneous amplitude and phase modulating metasurfaces consist of Si pillars of rectangular cross-section (acting as half-wave plates with length L_x and width L_y pairs ranging from $0.15p_i$ to $0.85p_i$, where p_i pitch of the unit cell. For each discrete wavelength λ_i , the corresponding value of p_i is shown in Suppl. Fig. S9. In addition, the transmission amplitude at each discrete wavelength λ_i , is conferred through rotation

angle θ of the nanopillar half-wave plates. Using the same v to x mapping, the corresponding lateral location dependent size of rotated rectangles ($L_x(x), L_y(x)$) and their rotation $\theta(x)$ determine the final metasurface layout to achieve simultaneous amplitude and phase modulation.

Experimental setup:

In the Fourier transform setup for this study, an optical pulse is first angularly dispersed by a grating into the first diffraction order, and then focused by an off-axis metallic parabolic mirror. The input beam has a diameter of 2 cm. The grating is blazed with 300 grooves/mm. The parabolic mirror has a reflected focal length of 381 mm, with an off-axis angle of 15 °. The grating-parabolic mirror-pair is used to spatially disperse the optical pulse over the full length of one or more cascaded metasurfaces, following a quasi-linear function $\lambda(x)$. The beam size and grating combine to give a grating resolvance $R = 200 \text{ mm} \times 300 \text{ grooves/mm} = 6000$, which corresponds to a wavelength resolution of about 0.13 nm at the center wavelength of 800 nm. Under ray tracing, the astigmatism-limited spot size near focus, along the x-direction, is approximately 0.02 mm, as shown in Suppl. Fig. S1. This spot size corresponds to a wavelength resolution of about 0.16 nm after considering the function $\lambda(x)$ as shown in Fig. S2. Along the y-direction, the largest astigmatism-limited spot at the edge of the spectrum is approximately 0.2 mm. The effective numerical aperture of the parabolic mirror is $NA = 0.026$, which leads to a diffraction-limited spot size of $0.61\lambda/NA = 0.018 \text{ mm}$ at the center wavelength of $\lambda = 800 \text{ nm}$. We conservatively estimate that the accumulation of these non-idealities leads to an effective monochromatic spot size of approximately 0.037 mm, which corresponds to a wavelength resolution of about 0.33 nm or a frequency resolution of 150 GHz.

Metasurface devices are inserted within the focal volume about the Fourier plane to help achieve the required net masking function. After passing through the metasurfaces, the beam is recombined using a second parabolic mirror and grating pair, yielding a shape-modified pulse of desired temporal characteristics. The metasurfaces are illuminated using a Ti:Sapphire oscillator generating $\lesssim 10 \text{ fs}$ pulses, centered at 800 nm (FWHM bandwidth of $\approx 60 \text{ THz}$), with a repetition rate of 75 MHz. The characteristics of the recombined pulse exiting the system, *i.e.* spectral amplitude and phase, are measured using the SPIDER technique (34).

Supplementary Text

Jones Matrix for independent amplitude & phase modulation:

We assume that an input light polarized along the x -axis first passes through an optical element described by a Jones matrix J_s and then a linear polarizer aligned to transmit x -polarized light. The final polarization state of the output light can be given by:

$$\begin{pmatrix} te^{j\varphi} \\ 0 \end{pmatrix} = \begin{pmatrix} 1 & 0 \\ 0 & 0 \end{pmatrix} J_s \begin{pmatrix} 1 \\ 0 \end{pmatrix} = \begin{pmatrix} 1 & 0 \\ 0 & 0 \end{pmatrix} \begin{pmatrix} J_{11} & J_{12} \\ J_{21} & J_{22} \end{pmatrix} \begin{pmatrix} 1 \\ 0 \end{pmatrix}, \quad (\text{S1})$$

where $te^{j\varphi}$ is the complex amplitude of the masking function a specific frequency component. Multiplying out the matrices gives:

$$\begin{pmatrix} te^{j\varphi} \\ 0 \end{pmatrix} = \begin{pmatrix} J_{11} \\ 0 \end{pmatrix}. \quad (\text{S2})$$

Now consider a birefringent metasurface element with the fast(slow) axis aligned along the $x(y)$ direction. It can be described by a diagonal Jones matrix:

$$\mathbf{M}_0 = \begin{pmatrix} M_{11} & 0 \\ 0 & M_{22} \end{pmatrix} = \begin{pmatrix} e^{j\varphi_x} & 0 \\ 0 & e^{j\varphi_y} \end{pmatrix}, \quad (\text{S3})$$

where M_{11} and M_{22} are the complex transmission coefficients for the x - and y -polarized light. Now if the birefringent element is rotated counter-clockwise by an angle θ , the resulting Jones matrix is then given by:

$$\mathbf{M}(\theta) = \mathbf{R}(-\theta)\mathbf{M}_0\mathbf{R}(\theta) = \begin{pmatrix} \cos \theta & -\sin \theta \\ \sin \theta & \cos \theta \end{pmatrix} \begin{pmatrix} e^{j\varphi_x} & 0 \\ 0 & e^{j\varphi_y} \end{pmatrix} \begin{pmatrix} \cos \theta & \sin \theta \\ -\sin \theta & \cos \theta \end{pmatrix}, \quad (\text{S4})$$

where $\mathbf{R}(\theta)$ is the rotation matrix. Inserting (S4) into (S1) then yields:

$$te^{j\varphi} = J_{11} = e^{j\varphi_x}\cos^2\theta + e^{j\varphi_y}\sin^2\theta. \quad (\text{S5})$$

Finally, consider the special case when the birefringent metasurface element represents a half-wave plate by enforcing:

$$\frac{e^{j\varphi_x}}{e^{j\varphi_y}} = e^{\pm j\pi} = -1. \quad (\text{S6})$$

Inserting (S6) into (S5) yields:

$$te^{j\varphi} = e^{j\varphi_x}(\cos^2\theta - \sin^2\theta) = \cos(2\theta)e^{j\varphi_x}. \quad (\text{S7})$$

Note that for the designed metasurface/polarizer combination, the amplitude of the transmission coefficient is solely determined by rotation angle θ via $t = \cos(2\theta)$ and the phase of that is determined by the pillar length L_x and width L_y through the color map of Fig. 3D.

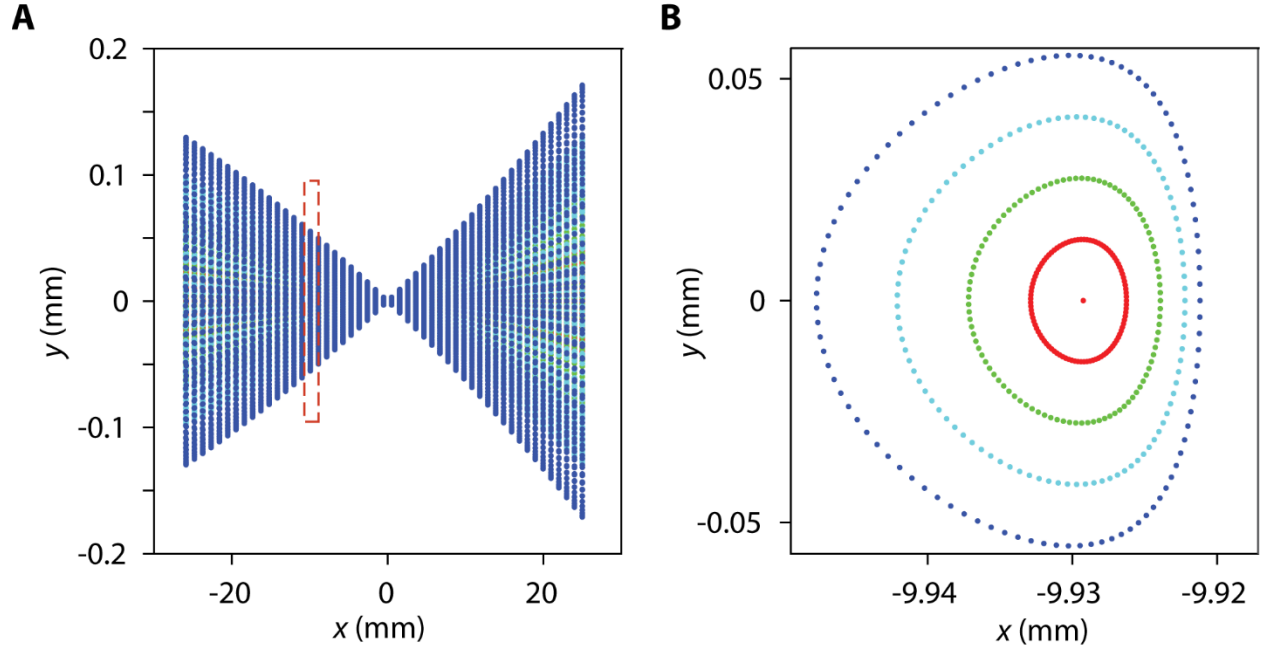


Fig. S1. Ray tracing spot diagrams of the optical setup. The frequency component at 800 nm is assumed to strike the mirror along the optical axis. **(A)** A spot diagram showing astigmatism-limited spots near focus for light of wavelengths between 580 nm (right-most spots, near $x = 25$ mm) and 1024 nm (left-most spots, near $x = -25$ mm). These individual spot diagrams, for various wavelengths, appear as vertical lines because of the greatly different scaling of the x and y axes. **(B)** A representative zoomed-in spot diagram for an incident beam of radius 1 cm at a wavelength of 886 nm (a zoomed version of the dashed red box in **(A)** near $x = -10$ mm). The red, green, light blue, and dark blue spots represent rays at a position of 0.25, 0.5, 0.75, and 1.0 times the radius of the incident beam, respectively.

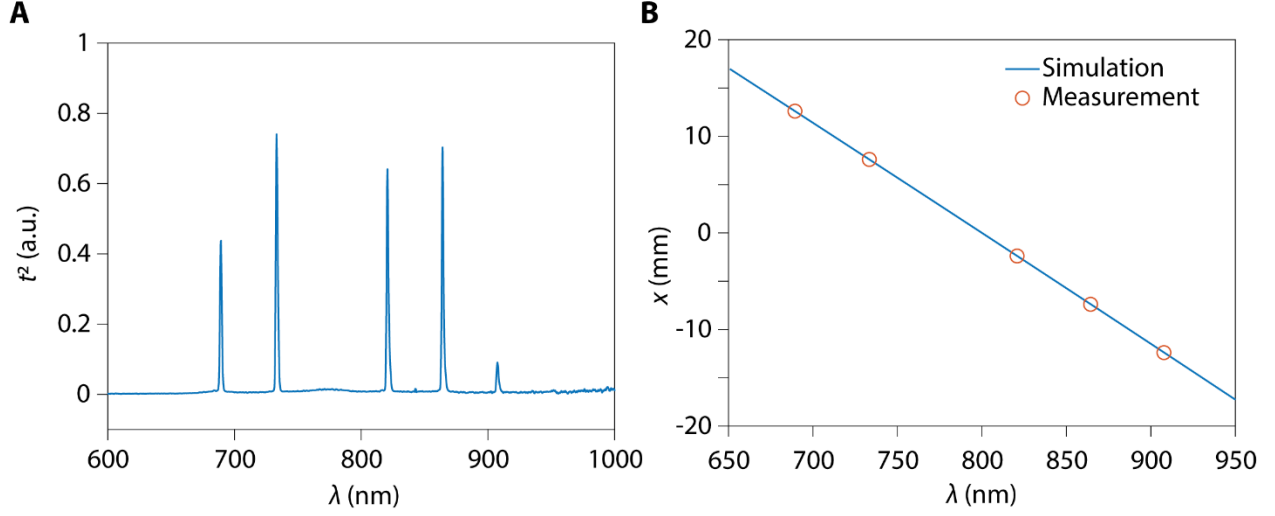


Fig. S2. Quasi-linear mapping of $\lambda(x)$. (A) Representative spectrum of the pulse transmitted through a reference modulation mask consisting of two sets of pinholes, each having two or three holes, respectively. The numbers of holes in each group are asymmetric for the ease of calibration. The hole pitch for each group is 5 mm. The reference modulation mask was translated along the x -axis at multiple locations to confirm the mapping of $\lambda(x)$. (B) The calibrated relation between x -position and wavelength λ at the Fourier plane. The red circles correspond to the peaks in (A) and the blue line corresponds to the simulated $\lambda(x)$ of the optical system using ray tracing. $\lambda(x)$ can be fitted with a linear function $\lambda(x) = -8.78 \text{ nm/mm} \cdot x + 800 \text{ nm}$.

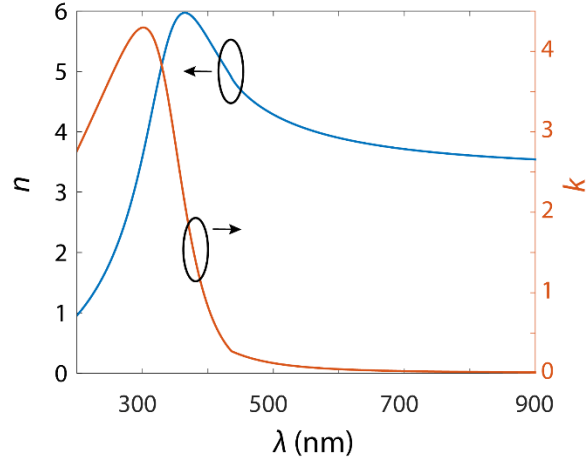


Fig. S3. Refractive index of polycrystalline silicon. The real (n) and imaginary part (k) of the refractive index of LPCVD Si, deposited on an oxide coated reference Si substrate (thermal oxide thickness = 300 nm), and measured using spectroscopic ellipsometry. The values for both n and k are within 2 % corresponding to one standard deviation in the ellipsometry measurement.

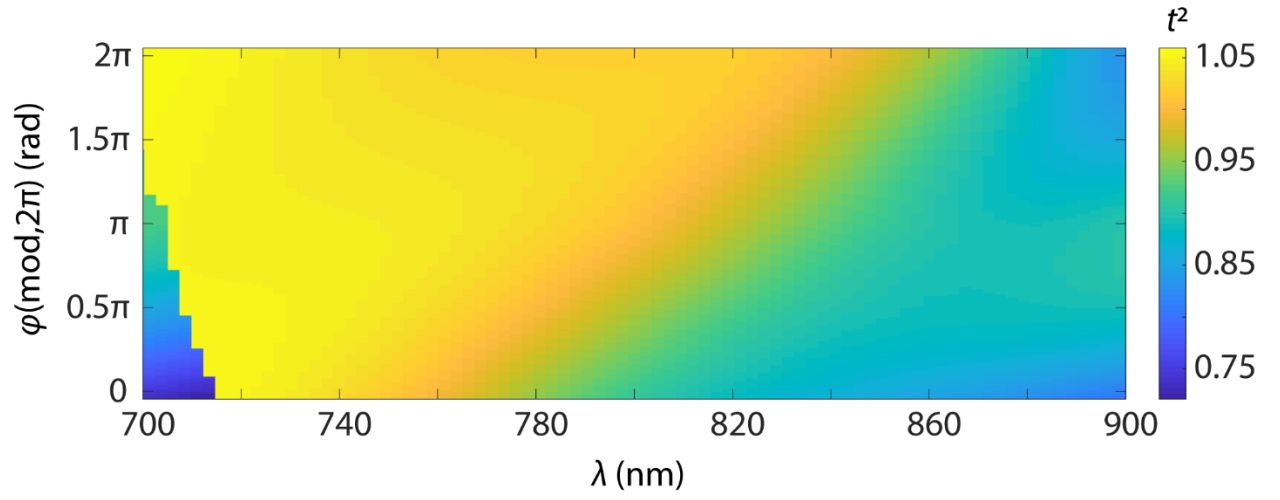


Fig. S4. Color-map of the calculated amplitude transmission coefficient t^2 . Calculated t^2 corresponding to the phase-manipulating metasurfaces discussed in Fig. 2. The transmission amplitude remains $> 70\%$ for any choice of L (required to achieve an arbitrary phase $\varphi(\text{mod}, 2\pi)$ at any wavelength λ) in the phase manipulating metasurface.

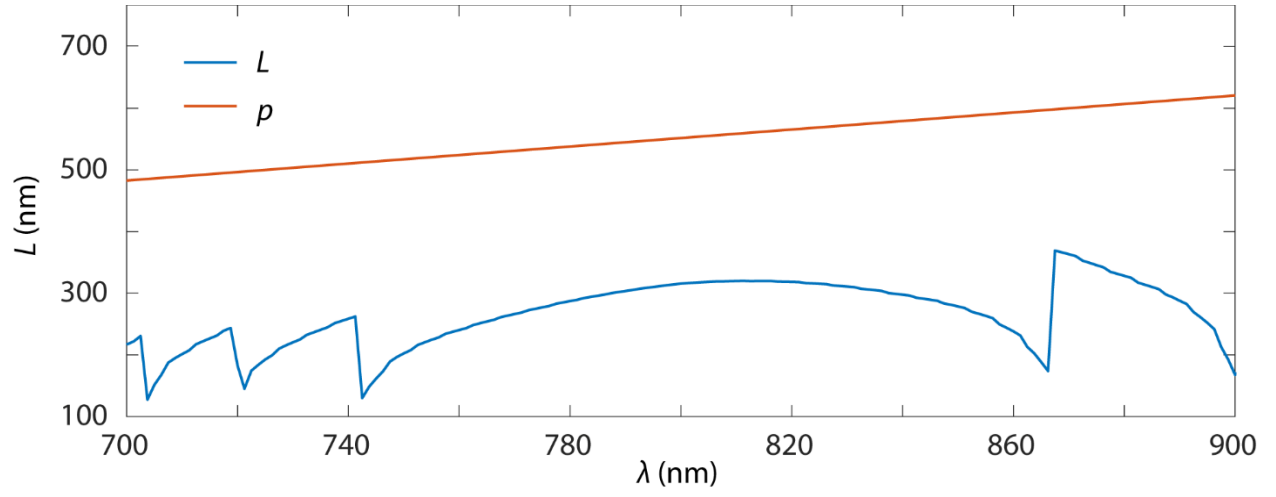


Fig. S5. Side-length L of the nanopillar and lattice constant p vs. the wavelength λ . Retrieved using the procedure described in Methods to achieve the quadratic spectral phase plotted in Fig. 2C.

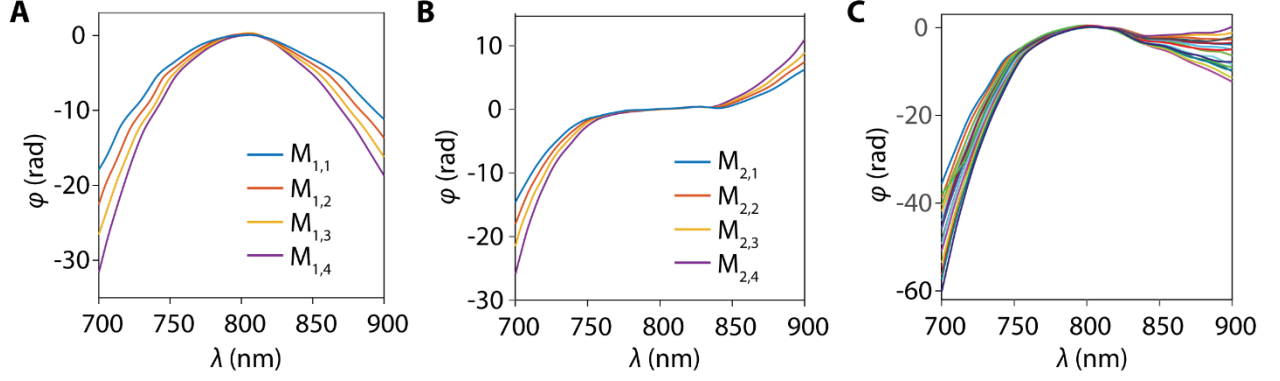


Fig. S6. Targeted designs for cascading phase manipulating metasurfaces. (A) Targetd (B) Targetd Four quadratic masking functions $m_{1,j}(x) = e^{i\varphi_{1,j}(\nu(x))}$ ($j = 1, 2, 3$, and 4) implemented on S_1 , where $\varphi_{1,j}(\nu) = -A_{1,j}(\nu - \nu_0)^2$, $A_{1,1} = 6 \times 10^{-3}$ rad/THz², $A_{1,2} = 7 \times 10^{-3}$ rad/THz², $A_{1,3} = 8 \times 10^{-3}$ rad/THz², and $A_{1,4} = 9 \times 10^{-3}$ rad/THz². (B) Four cubic masking functions $m_{2,j}(x) = e^{i\varphi_{2,j}(\nu(x))}$ ($j = 1, 2, 3$, and 4) implemented on S_2 , where $\varphi_{2,j}(\nu) = -A_{2,j}(\nu - \nu_0)^3$, $A_{2,1} = 7 \times 10^{-5}$ rad/THz³, $A_{2,2} = 9 \times 10^{-5}$ rad/THz³, $A_{2,3} = 1.1 \times 10^{-4}$ rad/THz³, and $A_{2,4} = 1.3 \times 10^{-4}$ rad/THz³. (C) 16 spectral phase shift masking functions available through cascading S_1 and S_2 .

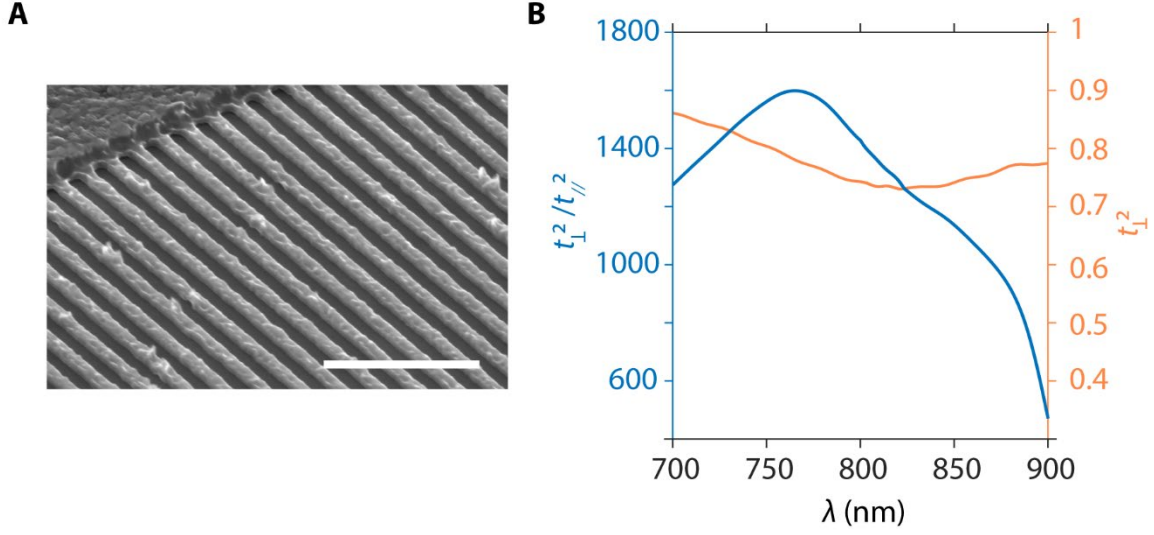


Fig. S7. Experimental characterization of the thin-film wire-grid polarizer designed for the simultaneous phase and amplitude manipulating metasurface discussed in Fig. 3. (A) A representative SEM image (52 ° perspective view) of the wire polarizer fabricated for this study. The polarizer wires consist of 200 nm-wide and 500 μm -long Al nanowires, positioned in a one-dimensional lattice with pitch of 200 nm along the x -direction. Scale bar represents 1 μm . (B) Experimentally measured extinction ratio ($t_{\perp}^2/t_{\parallel}^2$) and relative power transmittance t_{\perp}^2 vs. the wavelength λ of the wire polarizer, where t_{\perp}^2 is the power transmittance for the input-polarization orthogonal to the wires and t_{\parallel}^2 is that for the polarization parallel to the wires.

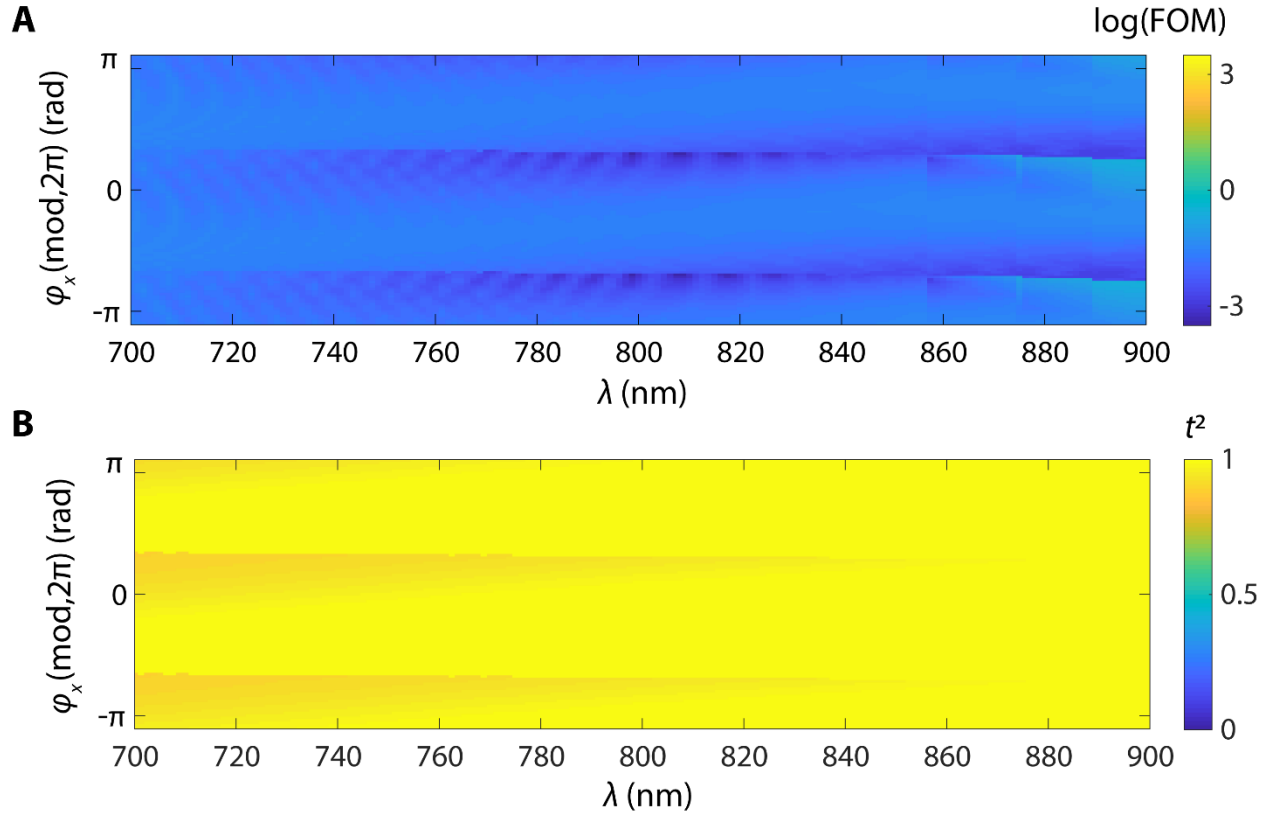


Fig. S8. Color-map of the calculated FOM and transmission coefficient t_x^2 for the phase & amplitude modulation mask design. (A, B) Color-maps depicting the FOM and relative transmission intensity t^2 respectively, vs. the wavelength λ for any arbitrary phase $\varphi_x \pmod{2\pi}$ at any wavelength, calculated for corresponding L_x and L_y pair values used in Fig. 3D.

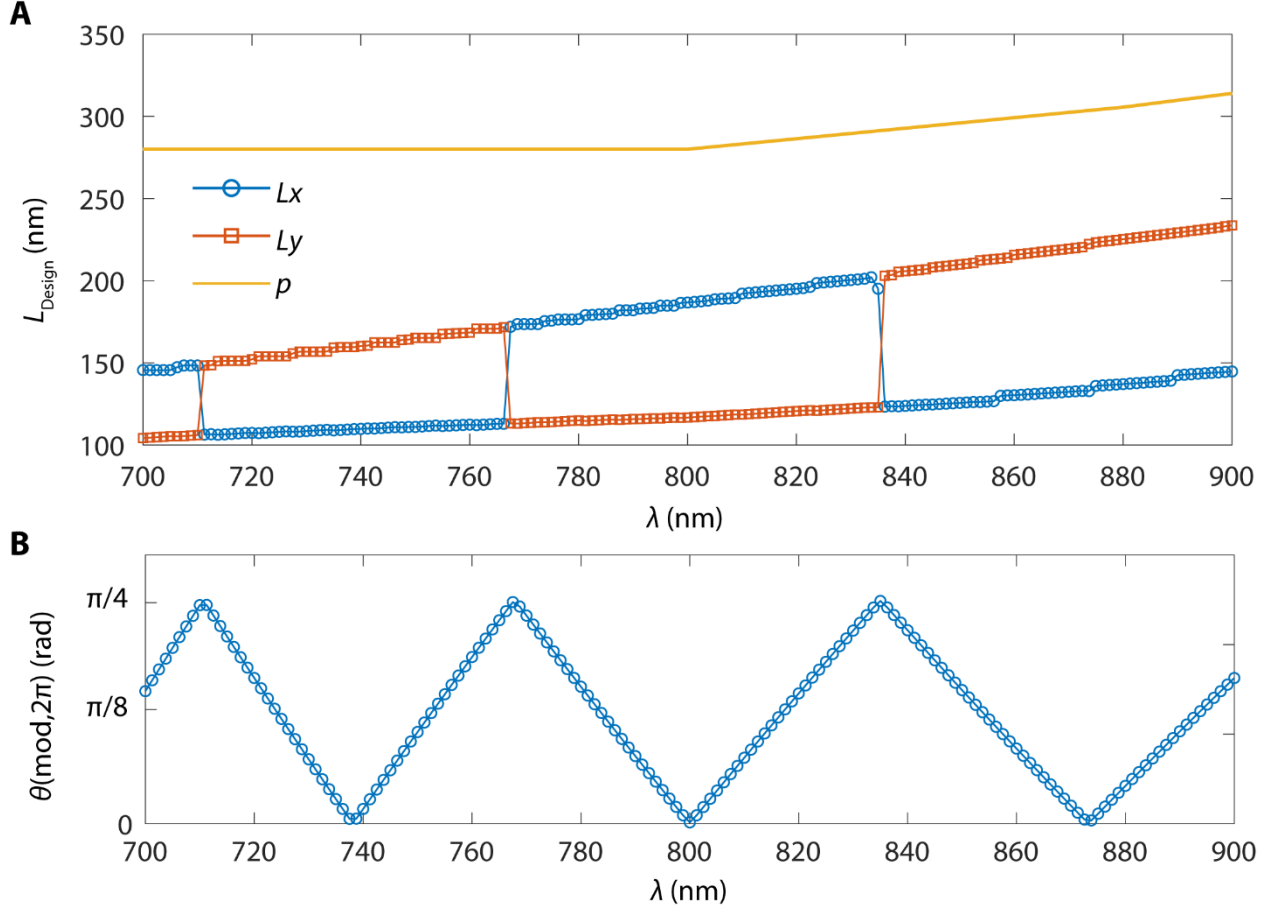


Fig. S9. Layout design parameters for the pulse splitting metasurface. (A) Rectangular nanopillar length L_x and width L_y for each wavelength λ_k along with k -th corresponding pitch p_k used to implement the required phase function in Fig. 3E. The pitch p was optimized for 2π coverage at five wavelengths 700 nm, 750 nm, 800 nm, 840 nm, and 900 nm within the pulse bandwidth, and p_k at each λ_k was determined through interpolation. L_x , L_y pairs are determined using the procedure described in the Methods section. (B) Rotation angle of the nanopillars θ_k for each wavelength λ_k to implement the targeted amplitude function of Fig. 3F.